



Article

About the Use of Concrete Damage Plasticity for Modeling Masonry Post-Elastic Behavior

Luigi Salvatore Rainone ¹, Vito Tateo ¹, Siro Casolo ²  and Giuseppina Uva ^{1,*} 

¹ DICATECH Department, Politecnico di Bari, 70125 Bari, Italy; l.rainone@studenti.poliba.it (L.S.R.); vito.tateo@polimi.it (V.T.)

² ABC Department, Politecnico di Milano, 20133 Milano, Italy; siro.casolo@polimi.it

* Correspondence: giuseppina.uva@poliba.it; Tel.: +39-805963832

Abstract: Considering the high vulnerability of existing masonry buildings, which often have strategic or cultural value, professionals and specialized engineers are frequently required to model complex historical buildings. The approaches proposed by National Building Codes may not always be suitable for such cases, but more detailed approaches are necessary, relying on FEM continuum modeling and inelastic constitutive law. There are many constitutive laws proposed in the literature that allow us to accurately reproduce the mechanical behavior of masonry. However, they require the identification of several parameters that are not easy to determine. In this study, a sensitivity analysis of the parameters of a nonlinear constitutive law very popular for masonry modeling (the “Concrete Damage Plasticity—CDP” model) is conducted, considering literature tests of masonry panels under shear stress as the benchmark. The aim is to assess the influence of the main parameters of the model and compare them to one of the more commonly used Mohr–Coulomb failure criteria.

Keywords: masonry; FEM; concrete damage plasticity; sensitivity analysis; dilatancy; post elastic behavior



Citation: Rainone, L.S.; Tateo, V.; Casolo, S.; Uva, G. About the Use of Concrete Damage Plasticity for Modeling Masonry Post-Elastic Behavior. *Buildings* **2023**, *13*, 1915. <https://doi.org/10.3390/buildings13081915>

Academic Editor: Mohamed K. Ismail

Received: 1 July 2023

Revised: 16 July 2023

Accepted: 18 July 2023

Published: 27 July 2023



Copyright: © 2023 by the authors. Licensee MDPI, Basel, Switzerland. This article is an open access article distributed under the terms and conditions of the Creative Commons Attribution (CC BY) license (<https://creativecommons.org/licenses/by/4.0/>).

1. Introduction

The numerical modeling of masonry structures is a challenging issue because masonry is a composite material obtained by assembling blocks with or without an interposed layer of mortar. Blocks can be more or less regular, made of different materials such as stone, calcarenite, clay, or concrete, and assembled in one or more layers, according to regular patterns or chaotically. Around the world, there are different traditions, different materials available, and consequently, different masonry types [1,2].

Despite the diversity of masonry typologies, they all have some recurring peculiarities that have challenged researchers and technicians over the years. As a general feature, masonry can be classified as non-homogeneous, orthotropic, and brittle. These properties are related to the construction technology, i.e., the presence of a pattern of discrete blocks, that determines the material anisotropy. In general, for regular patterns, such as the running, the common, and the English or the Flemish bond, masonry walls have continuous horizontal joints and staggered vertical joints. This micro-structure, with the interposition of mortar layers, causes the masonry wall to respond differently depending on the direction of stress. Furthermore, since both mortar and blocks usually have a brittle response with limited tensile strength, the masonry also shows a brittle response. Moreover, an accurate model should also consider the large dispersion that characterizes the material strength, as reported by Gooch et al. [3].

In order to deal with these peculiarities, depending also on the scale of the analysis, different modeling strategies have been developed in the literature [4–9]. D’Altri et al. [10], and other authors in different applications [11], report a useful review that highlights the strengths and weaknesses of many different approaches. A major distinction is possible between micro models and homogeneous models. Different types of approaches belong

to the first family, depending on the formulation adopted and the interaction between the different masonry components. Some of these approaches are interface element-based approaches, contact-based approaches, textured continuum-based approaches, block-based limit analysis approaches, and extended finite element approaches [12–17]. Some of these approaches rely on the definition of specific laws to reproduce the masonry response, for example, the traction separation law for cohesive elements [18]. According to the micro-modeling strategy, a masonry wall is discretized in mortar and blocks, reproducing the wall texture and considering in this way its influence on the masonry elastic and post-elastic response. On one hand, it is easier to characterize masonry components than characterize composite masonry; on the other hand, the model and computational efforts are not negligible, especially at the building scale. In addition, at the building scale, it is improbable that the exact masonry texture at any point is known [10].

Homogeneous continuum approaches are based on a homogenization procedure that defines the continuum properties of masonry both for the elastic and the post-elastic response. The response of the homogeneous material can be defined through constitutive behavior based on experimental results or a multi-scale procedure, in which the homogeneous properties are defined in each step of the analysis from an RVE micro-model [19–33]. In the field of homogeneous models, complex constitutive models have been developed to account for any aspect of masonry behavior [34–36]. These models require the definition of several parameters that are not easy to determine, especially in the case of existing buildings and historical sites. In order to overcome the limitations of a homogenization procedure that do not allow us to consider the texture effects on the masonry response, some authors [37,38] have also developed approaches based on enriched kinematics, e.g., by exploiting the peculiarities of the Cosserat micropolar theory. These models allow us to account for the size effect and implicit non-local behavior that depend on the shape and the stiffness of the blocks at the macro-scale through the definition of a homogeneous Cosserat material.

In the field of finite elements approaches, considering the brittle behavior of masonry and of its components, many authors have adopted a constitutive behavior based on Concrete Damage Plasticity (hereafter, CDP). This model was first developed for modeling concrete [39,40] and through the years has also found application in modeling high-strain events such as blast and impact loads [41,42]. Later, it has been also applied to the study of masonry structures, both for micro models [43–47] and for homogeneous models [48–56]. There are a number of constitutive models available in the libraries of commercial FE software for masonry, which, drawing on decades of studies and advances in the field of masonry mechanics, all have in common the ability to effectively describe the highly nonlinear behavior, plasticity and damage development, and hysteretic dissipation that characterizes such a material. Leaving aside the discussion of which software or model provides the best performance, a major issue of complex constitutive laws such as CDP is the necessity of defining a large set of parameters, which, in the case of masonry materials, and especially dealing with vulnerability assessment by homogeneous approaches, are very difficult to evaluate by experimental tests. In the absence of data, there are two possible strategies: To adopt parameters that have been already calibrated for concrete or specifically calibrate those parameters on an experimental curve, after a fitting analysis [57].

In this study, after a brief introduction to CDP peculiarities and parameters, the parameters have been compared with one of the more common Mohr–Coulomb failure criteria in order to guide and study the influence of these parameters on the masonry model response. A sensitivity analysis has been conducted on the CDP parameters, considering a well-known experimental shear test on a masonry wall available in the literature as the benchmark. The analyses have been conducted using both a micro-model and a homogeneous one (referred to as macro-model in the following), with the goal of understanding the influence of the CDP parameters on the response of the masonry panel and providing a rational approach that facilitates the choice of the right set of CDP parameters for any kind of masonry type in practical applications.

2. Concrete Damage Plasticity Model

The concrete damage plasticity material model has its theoretical roots in the theory of plasticity and damage mechanics [58]. Historically, its origins are in the analysis of concrete structures; however, as already pointed out in the introduction, it is often used to investigate the behavior of masonry structures with good results. It was originally developed by Lubliner et al. [39] and subsequently modified and improved by Lee and Fenves [40]. As stated by Lu et al. [59], to model the damage process, it is necessary to define a constitutive law in order to determine the stress–strain law, a yield criterion, a hardening law, and a flow rule to describe the post-elastic response and, in the end, a damage initiation criterion and a damage evolution law.

In the following, some of the constitutive behavior parameters will be presented.

2.1. Damage Parameters

Lubliner et al. proposed a material model based on a new yield criterion to account for both elastic and plastic loss of stiffness due to the occurrence of cracks. In fact, the formation of cracks is associated with dissipated energy and, consequently, with the damage process [40]. In general, the damaging process can affect different material properties, such as its anisotropy, its stiffness, or its strength [58]. Lubliner et al. [39] originally considered one scalar damage variable linked to stiffness. This damage variable was unique for all the stress states that concern the material.

Lee and Fenves [40] later pointed out that a single scalar damage variable was only useful for analyzing monotonic loading problems, but it was not useful for cyclic loading problems. In fact, in the latter problems, it was necessary to analyze the cyclic behavior of the material, which showed a different response under tensile and compressive loading. Therefore, they introduced two independent damage variables, which could separately consider tensile and compressive damage. For the uniaxial case, the scalar damage variable d reduces the elastic modulus according to the following equation [60]:

$$E = (1 - d) E_0, \quad (1)$$

where E_0 is the undamaged elastic modulus and d is the damage variable function of the compression and tensile damage variables d_c and d_t and of the parameters s_c and s_t that consider the stiffness recovery effects associated with stress reversals [60]:

$$(1 - d) = (1 - s_t d_c)(1 - s_c d_t) \quad (2)$$

d_c and d_t are functions of the tensile and compressive plastic strains, respectively, while s_c and s_t are functions of the stress state [60]:

$$s_t = 1 - w_t r^*(\sigma_{11}), \quad 0 \leq w_t \leq 1 \quad (3)$$

$$s_c = 1 - w_c(1 - r^*(\sigma_{11})); \quad 0 \leq w_c \leq 1 \quad (4)$$

where the unit step function $r^*(\sigma_{11})$ is defined as follows [60]:

$$r^*(\sigma_{11}) = H(\sigma_{11}) = \begin{cases} 1 & \text{if } \sigma_{11} > 0 \\ 0 & \text{if } \sigma_{11} < 0 \end{cases} \quad (5)$$

w_c and w_t are weight factors introduced in order to control the recovery of the tensile and compressive stiffness when the load is reversed.

The strength and the damage are defined by the user to increase the values of the tensile and compressive plastic strain.

The relationships introduced above can be generalized for multiaxial stress states. In this case, the stress–strain relationships are governed by the scalar damage elasticity equation [60]:

$$\sigma = (1 - d)D_0^{el} : (\varepsilon - \varepsilon^{pl}) \quad (6)$$

where D_0^{el} is the elasticity matrix referred to as the initial condition, namely the undamaged one; ε is the strain tensor and ε^{pl} is the plastic part of the strain tensor, decomposing the strain tensor into elastic and plastic parts [40].

2.2. Yield Function and Its Parameters

The CDP yield function is a function of the effective stresses $\bar{\sigma}$, which consider that the crack formation leads to a reduction in the load-carrying area [61–63]. Hence, the effective stresses are always bigger than the stresses σ . The assigned tensile and compression yield stresses for different values of the inelastic strains are coherently scaled obtaining the effective uniaxial cohesion stresses [60]:

$$\begin{aligned} \bar{\sigma}_t &= \frac{\sigma_t}{1-d_t} \\ \bar{\sigma}_c &= \frac{\sigma_c}{1-d_c} \end{aligned} \quad (7)$$

The CDP yield function that considers a different evolution of strength under compression and tension was developed by Lee and Fenves [40]:

$$F(\bar{\sigma}, \tilde{\varepsilon}^{pl}) = \frac{1}{1-\alpha} (\bar{q} - 3\alpha\bar{p} + \beta(\tilde{\varepsilon}^{pl}) \langle \hat{\sigma}_{\max} \rangle - \gamma \langle -\hat{\sigma}_{\max} \rangle) - \bar{\sigma}_c(\tilde{\varepsilon}_c^{pl}) \quad (8)$$

where:

- \bar{p} is the effective hydrostatic pressure.
- \bar{q} is the Von Mises equivalent of effective stress.
- α is the function of the ratio between the initial equi-biaxial and uniaxial compressive yield stresses σ_{b0} and σ_{c0}

$$\alpha = \frac{\sigma_{b0}/\sigma_{c0} - 1}{2\sigma_{b0}/\sigma_{c0} - 1} \quad (9)$$

- $\beta(\tilde{\varepsilon}^{pl})$ is a function of the effective cohesion stresses, $\bar{\sigma}_t(\tilde{\varepsilon}_t^{pl})$ and $\bar{\sigma}_c(\tilde{\varepsilon}_c^{pl})$ (for the respective levels of plastic deformations $\tilde{\varepsilon}^{pl}$), and of α

$$\beta(\tilde{\varepsilon}^{pl}) = \frac{\bar{\sigma}_c(\tilde{\varepsilon}_c^{pl})}{\bar{\sigma}_t(\tilde{\varepsilon}_t^{pl})} (1 - \alpha) - (1 + \alpha) \quad (10)$$

- $\hat{\sigma}_{\max}$ is the maximum eigenvalue of the effective stress tensor, and the Macaulay brackets $\langle . \rangle$ return zero if the argument is negative and return the argument if it is positive.
- γ is a direct function of the K_c parameters defined as the ratio between the Von Mises equivalent effective stress on the tensile meridian \bar{q}_{TM} and on the compressive meridian \bar{q}_{CM} ; the closer it is to 1, the closer the yield surface is to a circle on the deviatoric plane.

$$\gamma = \frac{3(1 - K_c)}{2K_c - 1} \quad (11)$$

Comparing Equation (8) with the Drucker Prager yield function or the Mohr–Coulomb one, always expressed in terms of p and q , it is evident that the α parameter can be related to the φ parameter of Mohr–Coulomb, defining the slope of the $p - q$ curve in the $p - q$ plane.

The cohesion compressive stress $\bar{\sigma}_c(\tilde{\epsilon}_c^{pl})$ and the $\beta(\tilde{\epsilon}^{pl})$ parameter instead shift the $p - q$ curve, similar to the cohesion in a Mohr–Coulomb criterion. In detail, the bigger $\beta(\tilde{\epsilon}^{pl})$ is, the lower is the yielding curve, and the bigger $\beta(\tilde{\epsilon}^{pl})$ is, the lower the tensile strength $\bar{\sigma}_t(\tilde{\epsilon}_t^{pl})$.

In the end, the γ parameter affects the yield surface similar to the $\beta(\tilde{\epsilon}^{pl})$ parameter, but only in the case of triaxial compression, i.e., when $\hat{\sigma}_{\max} < 0$. Different from the $\beta(\tilde{\epsilon}^{pl})$ portion, the γ parameter shifts the $p - q$ curve to higher values, coherently with a $K_c < 1$.

2.3. Dilation Angle

This constitutive model assumes a non-associated potential flow with the Drucker–Prager hyperbolic function as flow potential G [60]:

$$G = \sqrt{(\in \sigma_{t0} \tan \psi)^2 + q^2} - \bar{p} \tan \psi \quad (12)$$

where ψ is the dilation angle measured in the $p - q$ plane at high confining pressures (Figure 1); $\sigma_{t0}(\theta, f_i) = \sigma_t$ for $\bar{\epsilon}_t^{pl} = 0$ and $\bar{\epsilon}_t^{pl} = 0$ is the uniaxial tensile stress at failure, taken from the user-specified tension stiffening data; \in is the eccentricity, which defines the rate at which the function approaches the asymptote (the flow potential tends to be a straight line as the eccentricity tends to zero). A high value of \in corresponds to high curvature of the flow potential. Considering that the flow potential defines the plastic deformations $\dot{\epsilon}^{pl}$ through the following equation [60]:

$$\dot{\epsilon}^{pl} = \lambda \frac{\partial G(\bar{\sigma})}{\partial \bar{\sigma}} \quad (13)$$

where λ is a scalar hardening parameter [64].

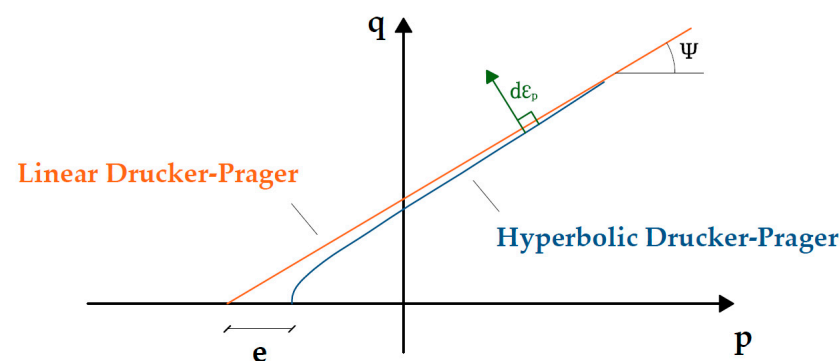


Figure 1. Linear and hyperbolic Drucker–Prager non-associated plastic flow potential in the $p - q$ plane.

In fact, the vector of the increment of plastic deformation $\dot{\epsilon}^{pl}$ has to be normal to the flow potential. Hence, the slope of the flow potential in the $p - q$ plane is the same as the increment of plastic deformation if decomposed in volumetric and shear components. Upon decomposing the plastic deformation in volumetric and shear deformation, the dilatancy indicates the attitude of a material to develop volume changes (namely plastic volumetric strain) during plastic shearing [64]. In fact, if $\psi = 0$, the material is incompressible, and if $\psi > 0$, the material dilates [65]. However, it is important to highlight that the dilation angle has no effect on the material strength, which is different from what happens in the Drucker–Prager or Mohr–Coulomb criteria, which have an associated potential flow so the dilation angle is equal to the friction angle because the flow potential coincides with the yield function. However, the dilatancy, if constrained, may lead to a modification of the stress state with an increase in p and, consequently, the material strength.

2.4. Viscosity Parameter

In order to overcome convergence issues due to the softening behavior, viscoplastic regularization has been implemented in the CDP constitutive equations. The visco-plasticity allows the stress state to be outside the yield surface. The parameter that regulates this behavior is the viscosity parameter μ , which represents the relaxation time of the viscoplastic system. In the CDP, a generalization of the Duvaut–Lions regularization was adopted. With this generalization, the viscoplastic strain rate tensor $\dot{\epsilon}_v^{pl}$ is the function of the difference between the stress tensor σ and the stress tensor σ^* corresponding to the effective stress tensor on the yield surface for the current strain ϵ [60]:

$$\dot{\epsilon}_v^{pl} = \frac{1}{\mu} D^{el-1} : (\sigma - \sigma^*) \quad \text{with } \sigma^* = \bar{\sigma}(1-d) \quad \text{and} \quad \sigma = D^{el} : (\epsilon - \epsilon_v^{pl}) \quad (14)$$

The viscoplastic strain rate tensor can also be written in terms of the plastic strain evaluated in the inviscid model ϵ^{pl} and the viscoplastic strain ϵ_v^{pl} [60]:

$$\dot{\epsilon}_v^{pl} = \frac{1}{\mu} (\dot{\epsilon}^{pl} - \dot{\epsilon}_v^{pl}) \quad (15)$$

Neglecting the effects of viscosity on the damage parameters, the stress tensor–strain relation can be written in the following form [60]:

$$\sigma = (1-d)D_0^{el} : (\epsilon - \epsilon_v^{pl}) = \sigma^* + \mu D^{el} \dot{\epsilon}_v^{pl} \quad (16)$$

Hence, the effects of the viscosity strain rate on the stresses are bigger the bigger μ is. As highlighted by previous authors, it can considerably change the results [66,67].

3. Case Study

The experimental results obtained by Raijmakers and Vermeltfoort (1992,1993) and CUR (1994) [68–70] on shear walls have been considered a benchmark to study the influence of CDP parameters on the numerical results. Considering that the tests were run in Eindhoven, in the following sections, they will be called “Eindhoven walls”.

In the literature cited above, several experimental results are available regarding different masonry walls with different geometrical characteristics and different boundary conditions applied. The test group of JxD panels is composed of four different walls with the same geometry, without openings and with different vertical loads applied at the top of each wall. These are identified by the acronyms J4D, J5D, J6D, and J7D. All the walls are subjected to horizontal loading at the top with a displacement control procedure. For each panel, the authors reported the registered crack pattern, the force–displacement curve, and the mechanical properties of mortar and blocks.

The bottom of the wall is effectively fixed to the ground, while at the top, after the application of the vertical load, the vertical displacements are constrained in order to avoid overturning phenomena. Figure 2 reports the boundary conditions for the lateral loading phase and the crack pattern registered in the J4D test with a prestressing load equal to 0.30 Mpa. All the walls of the JxD test group have dimensions of $0.99 \times 1.00 \text{ m}^2$ and are characterized by the presence of 18 total courses. Sixteen of them are active and two of them are fixed, each one in a steel beam.

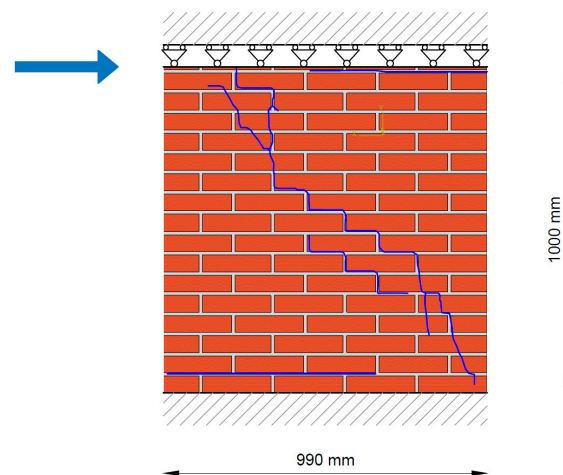


Figure 2. Eindhoven shear wall: Geometrical features, boundary conditions, and map of damage for the J4D test with a prestressing load of 0.3 MPa.

With regard to the masonry texture and components, the bed and vertical joints are filled with mortar and are 0.01 m thick. The mortar is made with a volumetric ratio of cement: lime: sand equal to 1:2:9 [4]. Blocks are wire-cut solid clay bricks with dimensions of 0.21 m \times 0.052 m \times 0.1 m. The mechanical properties of the masonry components can be retrieved from the literature [26] as shown in Table 1.

Table 1. Mechanical properties of the mortar and of the block unites (p is the pressure applied; E is Young's modulus; ν is Poisson's ratio; σ_t and σ_c are the tensile and compressive strengths; G'_t and G'_c are the tensile and compressive fracture energy; ϕ_f is the friction angle). It is worth noting that, for the block units, the parameters do not change with the pressure applied, and that some of them are not available.

Mortar							
P [MPa]	E [GPa]	ν	σ_t [MPa]	G'_t [J/m ²]	σ_c [MPa]	G'_c [J/m ²]	ϕ_f [°]
0.30	0.8	0.15	0.25	18	10.5	2800	36.9
1.21	1.0		0.16	12	11.5		
2.12	0.8		0.16	12	11.5		
Blocks							
E [GPa]	ν	σ_t [MPa]	G'_t [J/m ²]	σ_c [MPa]	G'_c [J/m ²]	ϕ_f [°]	
16.7	0.15	2	80	-	-	10	

The vertical loads for the different JxD walls are 0.30 MPa (J4D and J5D panels), 1.21 MPa (J6D panel), and 2.12 MPa (J7D panel). As shown in Figure 3, the magnitude of the vertical load leads to different results both in terms of damage and panel strength. In detail, upon increasing the vertical load, the cracks have fewer joints and the horizontal strength increases coherently with frictional behavior.

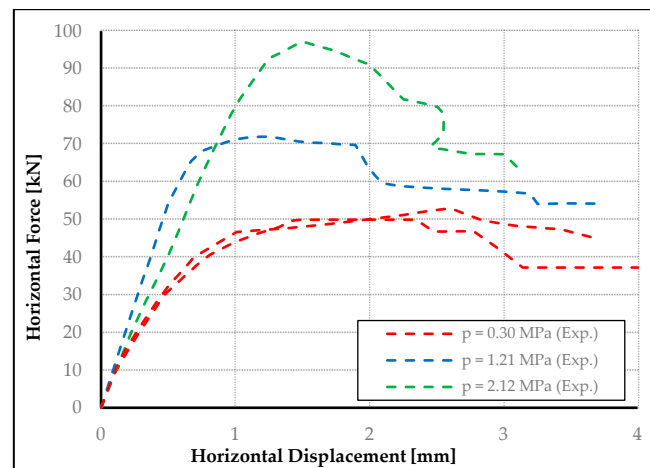


Figure 3. Experimental curves of Eindhoven shear walls under different prestressing loads [26].

4. Numerical Models

For numerical analyses, two FE models have been developed in Abaqus [60]. The first model is a micro-model implemented as a 3D panel discretized into partition faces and splitting the panel into blocks and mortar joints (Figure 4a). This micro-model is a continuous FE model in which the masonry texture is reproduced in detail by discretizing each block and mortar joint and assigning them different material properties. The interaction between mortar and blocks is a continuum. The second model is a homogeneous 3D FE model. In this case, only a homogeneous material was assigned to the entire panel (Figure 5). In both cases, the material model considered is the CDP; as already widely explained, this constitutive model requires several parameters. In the analyses, some parameters were kept fixed and others were modified one by one.

In order to reduce the influence of the mesh size on the tensile response, this was defined in terms of “direct cracking displacement” u_t^{ck} or “fracture energy” G_f . For a simple linear relation between stress and crack displacement, the two quantities can be easily related to obtain the cracking displacement corresponding to the total loss of strength, i.e., u_{t0} [60]:

$$u_{t0} = 2G_f / \sigma_{t0} \quad (17)$$

where σ_{t0} is the first tensile yield stress.

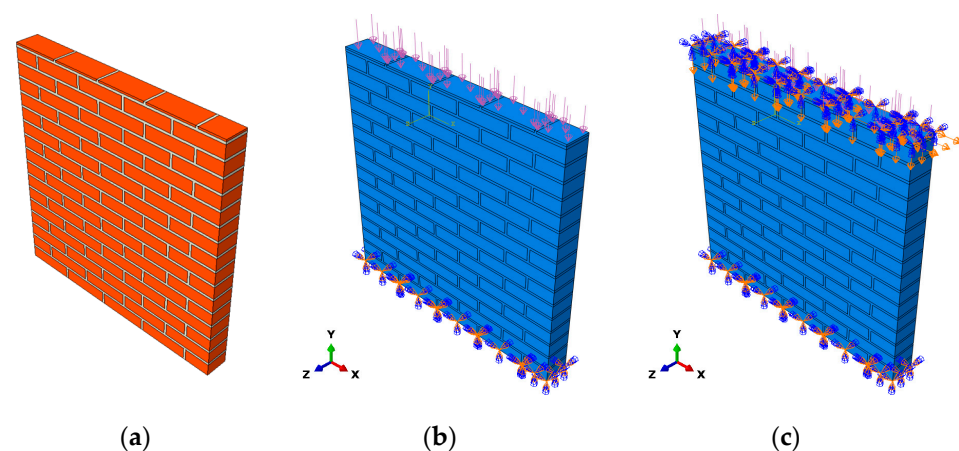


Figure 4. FE micro-model implemented in Abaqus: (a) View of the detailed definition of bricks and mortar joints (orange for bricks and white for joints); (b) application of the prestressing load at the top of the panel (pink arrows) and of the null displacement condition on the base; (c) application of the displacement conditions at the top of the panel for the shear test.

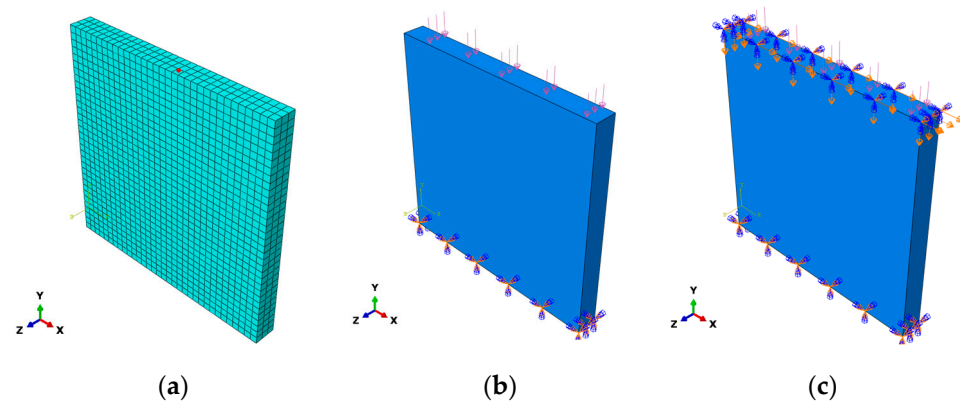


Figure 5. FE macro-model implemented in Abaqus: (a) Representation of the mesh size and the control point adopted for the construction of the capacity curves; (b) application of the prestressing load at the top of the model (pink arrows) and of the null displacement condition at the base; (c) application of the displacement conditions at the top of the panel for the shear test.

Coherently with the benchmark test, each model has first been subjected to a vertical and uniform pressure with a magnitude of 0.30 MPa at the top, and after, to a horizontal displacement of 0.0031 m applied to the top of the panel (Figure 4). The base of the panel is always fixed so a null displacement has been imposed in all directions. The vertical load and displacement have been applied to the model in two different steps. This means that, initially, the upper surface of the panel can move with certain displacement in the vertical direction under the vertical load. At the end of the application of the vertical load (first step), the actual value of the displacement is evaluated and applied as a boundary condition in the second step, keeping it constant throughout the second load step, in which horizontal displacement is applied. The upper face is constrained so that it can only move along the x-axis.

For the numerical models, different meshes have been considered. To limit the computational effort, a coarse mesh has been used by default (with an approximate global size of 3.0 cm). In some cases, the dimension of the smallest element has been reduced to 1.5 cm or to 1.0 cm (Figure 6) to analyze the influence of the mesh size on the results. In the following, each mesh density is indicated with “MESH” followed by “+” or “++” when the shown result is referring to a model characterized by a mesh finer than the default one.

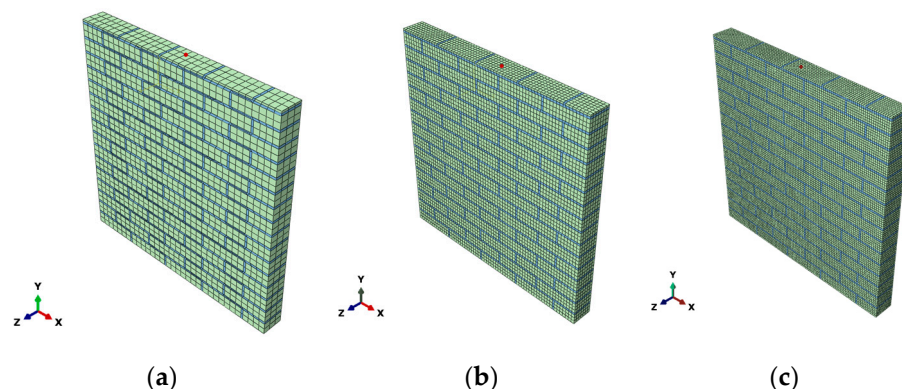


Figure 6. The different meshes created for the micro-models, with the representation of the control point adopted for the construction of the capacity curves: (a) Micro-model with average mesh size of 3 cm “MESH”; (b) micro-model with average mesh size of 1.5 cm “MESH +”; (c) micro-model with average mesh size of 1 cm “MESH ++”.

As already discussed, the influence of the main CDP parameters on the results was evaluated. Some of these parameters affect the plastic properties of the panel, the failure

criterion yielding surface, or the tensile behavior (both of the blocks and of the mortar). The influence of the prestressing load and the boundary conditions was also investigated. This is widely described in Section 5 for the micro-model and in Section 6 for the macro-model. For each analysis, the reaction force at the base has been plotted as a function of the horizontal displacement of the panel top.

5. Micro-Model Study

5.1. Sensitivity Analysis

Complex constitutive behaviors such as CDP require the definition of several parameters that are usually difficult to estimate experimentally due to the lack of knowledge that characterizes existing masonry buildings and the difficulties of testing existing masonry. Therefore, in this section, a sensitivity analysis is conducted, first to calibrate the model parameters on an experimental shear test but also to understand the influence of the material model parameters on the masonry response in order to provide some indications to facilitate calibration for any masonry type.

In this section, the influence of the following parameters on the micro-model results is investigated:

1. Dilation angle of the mortar.
2. Viscosity of blocks and mortar.
3. Mesh density.
4. Ratio of mortar yield stress σ_{b0}/σ_{c0} .

For the purposes of the research study, twenty-one models have been implemented. Twelve of these are aimed at analyzing the influence of the dilation angle on results (by using two different values of the viscosity parameter), five to investigate the mesh size, and four to determine the ratio between yielding compressive stress of the mortar.

In the analyses carried out, some parameters have been kept constant: Table 2 reports the values assumed for the masonry blocks and Table 2 reports the values adopted for the mortar joints, in agreement with the benchmark data and the literature values for CDP [48,55,60]. Other parameters have instead been considered variable, and the corresponding values will be specified in each paragraph. These parameters (already presented above) are tagged with “variable” in Table 2. It should be noted that when one of these parameters has been varied, the other variable parameters have been fixed assuming a value that will be specified each time.

Table 2. CDP reference parameters adopted for the mortar and the blocks.

Concrete Damage Plasticity for Mortar				
Elasticity parameters		E [Pa] 80,000,000		ν 0.15
Plasticity parameters	ψ [°] variable	ϵ 0.1	σ_{b0}/σ_{c0} variable	K 2/3 μ variable
Compressive response	Compressive strength [Pa]	Inelastic strain [%]	Damage parameter	Inelastic strain [%]
	9,450,000	0	0	0
	10,500,000	0.005	0.1	0.005
	0	0.015	0.2	0.015
Tensile response	Tensile strength [Pa]	Cracking displacement [m]	Damage parameter	Cracking displacement [m]
	250,000	0	0	0
	0	0.000144	0.1	0.000144

Table 2. Cont.

Concrete Damage Plasticity for Units					
Elasticity parameters	E [Pa] 3,128,000,000			ν 0.15	
Plasticity parameters	ψ [°] variable	ϵ_e 0.1	σ_{b0}/σ_{c0} variable	K 2/3	μ 0.0001
Compressive response	Compressive strength [Pa]	Inelastic strain [%]	Damage parameter	Inelastic strain [%]	
	13,000,000	0	0	0	
	17,500,000	0.004	0.1	0.005	
	0	0.01	0.2	0.015	
Tensile response	Tensile strength [Pa]	Cracking displacement [m]	Damage parameter	Cracking displacement [m]	
	variable	0	0	0	
	0	variable	0.1	variable	

5.1.1. Dilation Angle of the Mortar

At first, the influence of the dilation angle of the mortar on the capacity curve is analyzed. The parameters in Table 3 have been kept constant, and Table 4 reports the assumed values for the dilation angle. Moreover, for all the analyses, according to the benchmark test, the vertical displacements of the nodes at the top are constrained during the application of the horizontal displacement and a prestressing load of 0.30 MPa.

Table 3. Parameters set to analyze the influence of the dilation angle.

Fixed Parameters		
σ_{b0}/σ_{c0} 1.16	μ 0.002	Mesh size [cm] 3.00 (MESH)

Table 4. Values considered of the dilation angle.

Dilation Angle ψ					
5°	10°	15°	20°	30°	36.9°

The results are compared in terms of force–displacement curves (see Figure 7). From the comparison of the curves, it is possible to observe that the dilation angle does not change the position of the first yielding point in the curves because it does not change the yielding surface, but only affects the plastic strains. Instead, the post-elastic response changes considerably with the dilation angle, with an increasing hardening with the dilation angle. This increase in resistance can be explained by the confinement effect that the dilation together with the boundary conditions induces in the wall. It is also observed that for low values of dilatancy, the plastic branch is substantially straight, while the increase in dilatancy leads to an increase in the curvature of the branch, coherently with a modified status of the wall or of the material.

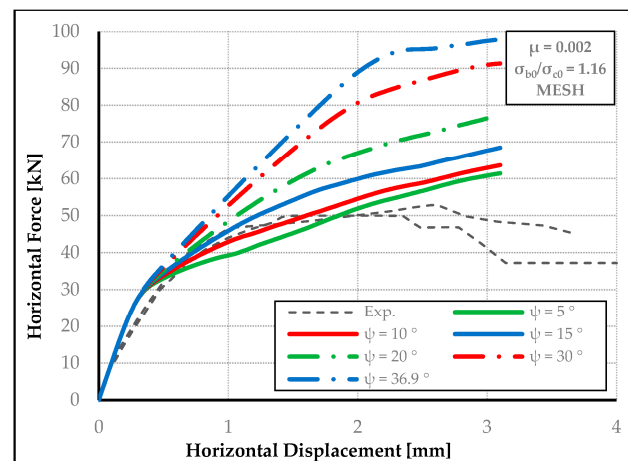
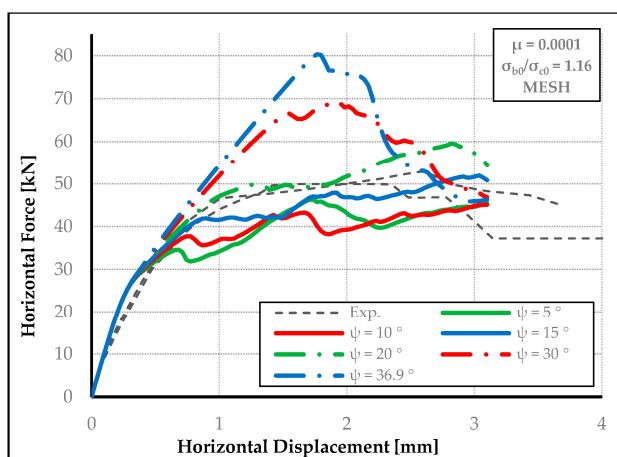


Figure 7. Force—displacement curves obtained from the analysis of micro-models for different dilation angles.

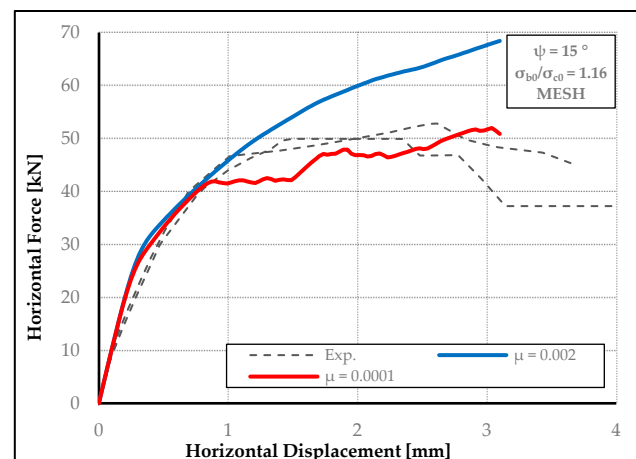
5.1.2. Viscosity Parameter

With the aim of analyzing the influence that the viscosity parameter has on the capacity curves, the analyses of the previous paragraph have been repeated, reducing the viscosity parameter to 0.0001.

The curves thus obtained differ considerably from the previous ones (Figure 8a). It is evident, in fact, that by decreasing the viscosity, the curves become less smooth, with some softening branches, which, for example, for 30° or 36.5°, correspond to the change in the post-elastic stiffness in Figure 7. In detail, Figure 8b highlights that, with the dilation angle set equal to 15°, the use of a viscosity parameter equal to 0.002 leads to an increased strength bigger than the 15% of the strength obtained with a viscosity parameter equal to 0.0001. It seems clear that a viscosity parameter equal to 0.002, which is the value usually adopted for analysis at the building scale, leads to a non-negligible overestimation of the material strength.



(a)



(b)

Figure 8. (a) Force—displacement curves obtained from the analysis of micro-models changing the dilation angle with the viscosity parameter equal to 0.0001; (b) comparison of the two response curves obtained for different viscosity parameters and dilation angle equal to 15°.

The influence of the viscosity parameter might be explained, considering the assigned tensile response, by the decreasing strength right after the yielding strength. As explained in Section 2.4, viscoplastic regularization allows the stress state to be outside the yielding

surface, and increasing the inelastic strain reduces its volume considering the assigned tensile and compressive laws. Hence, the viscosity always leads to an overstrength of the material, and its influence is bigger when the viscosity parameter is bigger.

In the end, Figure 8a shows that the curve corresponding to a dilation angle equal to 20° has an excellent fit with the benchmark curve.

5.1.3. Mesh Size

Considering the set of parameters for the CDP reported in Table 5, the influence of the mesh density has been analyzed, adopting the following average element sizes: 3 cm (MESH), 1.5 cm (MESH +), and 1 cm (MESH ++).

Table 5. Parameters set to analyze the influence of the mesh density.

Fixed Parameters		
$\psi [^\circ]$ 20°	μ 0.0001	σ_{b0}/σ_{c0} 1.16

Figure 9 shows that by increasing the number of elements, the post-elastic strength increases. This increase might be due to a different estimation of the plastic strains due to the dilatancy, coherently with a finer mesh. Hence, a finer mesh increases the overstrength associated with the dilatancy effect. In fact, comparing Figure 9a,b, obtained with dilation angles of 20° and 15° , respectively, it can be observed that in the first case, the difference between the curves is bigger than in the second one, proving that the observed increase in strength with the number of mesh elements is only a side effect of the dilatancy. In the end, in the case of micro-models for masonry for which it is known that the dilation of the mortar is bigger, it is necessary to adopt a finer mesh in order to accurately estimate the influence on results and obtain a precise damage pattern.

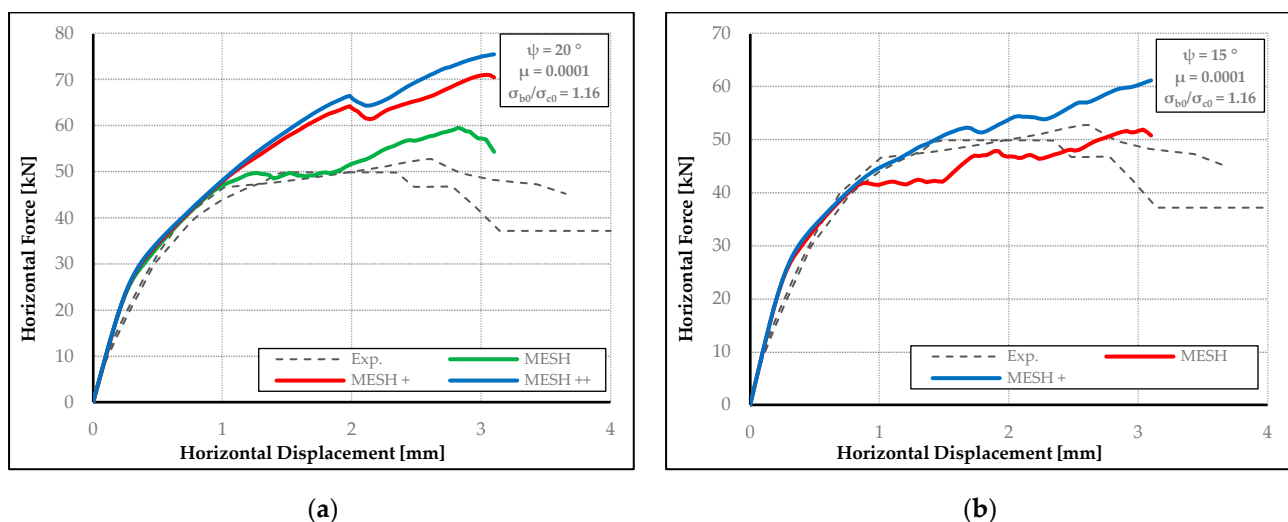


Figure 9. Capacity curves obtained from the analysis of micro-models with different mesh densities: (a) For a dilation angle equal to 20° and (b) for a dilation angle equal to 15° .

Figure 10 shows the damage maps under tension, which represent the crack pattern in the panel. First of all, it is important to highlight that damage maps do not significantly change with CDP parameters, and all maps reproduce the crack pattern experimentally registered in the Eindhoven panels well, even with the coarsest mesh. However, the damage obtained with the MESH+ model is more localized in mortar joints, affecting only some blocks locally, and better fits the experimental results. Despite better results having been obtained with a finer mesh, in order to reduce the computational effort, most of the further analyses have been conducted with the MESH model.

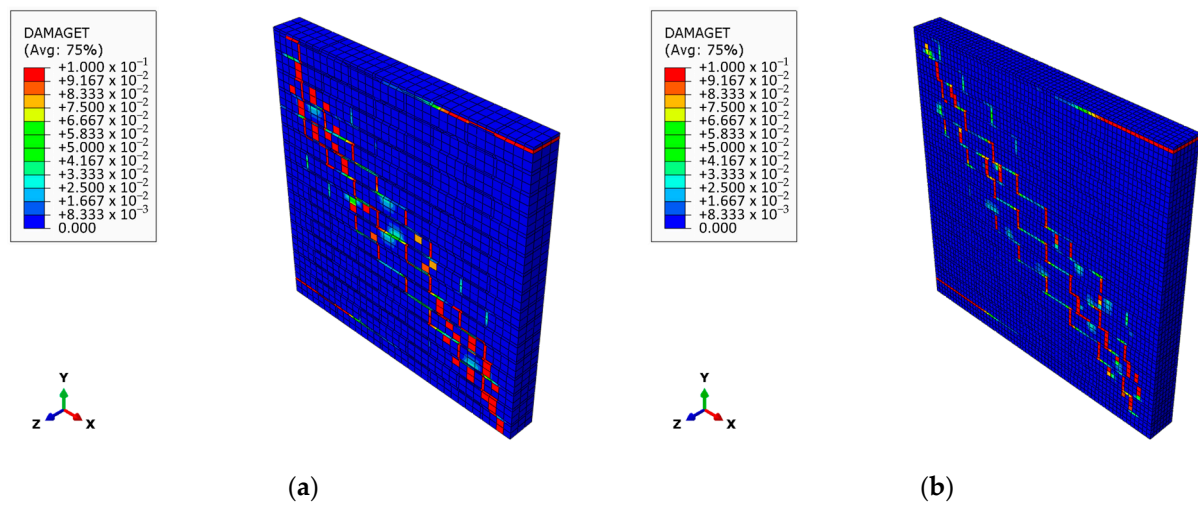


Figure 10. Map of the damage in tension developed in the micro-model referred to as (a) The green capacity curve of Figure 9 (MESH); (b) the red capacity curve of Figure 9 (MESH+).

5.1.4. Ratio between Yielding Compressive Stresses

In this paragraph, the influence of the ratio between the compressive yield stresses for uniaxial and equi-biaxial states is varied, changing the σ_{b0}/σ_{c0} ratio between 1.05, 1.16, 1.25, and 1.35 (Table 6). An equi-biaxial compressive yield stress is the yielding stress associated with a compressive stress state that in the principal reference system has $\sigma_{11} = \sigma_{22} = \sigma_{b0}$ and the other stress tensor components equal to zero. As explained in Section 2.1, this parameter, similar to the friction angle in the Mohr–Coulomb law, changes the slope of the yielding surface in the p–q plane. Table 7 reports the other parameters adopted for these analyses.

Table 6. Values considered for the ratio between compressive yielding stresses.

Ratio between Compressive Yielding Stresses σ_{b0}/σ_{c0}			
1.05	1.16	1.25	1.35

Table 7. Parameters set to analyze the influence of the ratio between compressive yielding stresses.

Fixed Parameters		
ψ [°]	μ	Mesh size [cm]
20°	0.0001	3.00 (MESH)

From the force–displacement curves (see Figure 11), it emerges that the response is not sensible regarding this parameter, and the curves almost overlap each other. Moreover, the first yielding point does not change considerably. This might be explained by the fact that the vertical load is small, and so the shear behavior of the wall is governed more by the cohesion than by the friction coefficient.

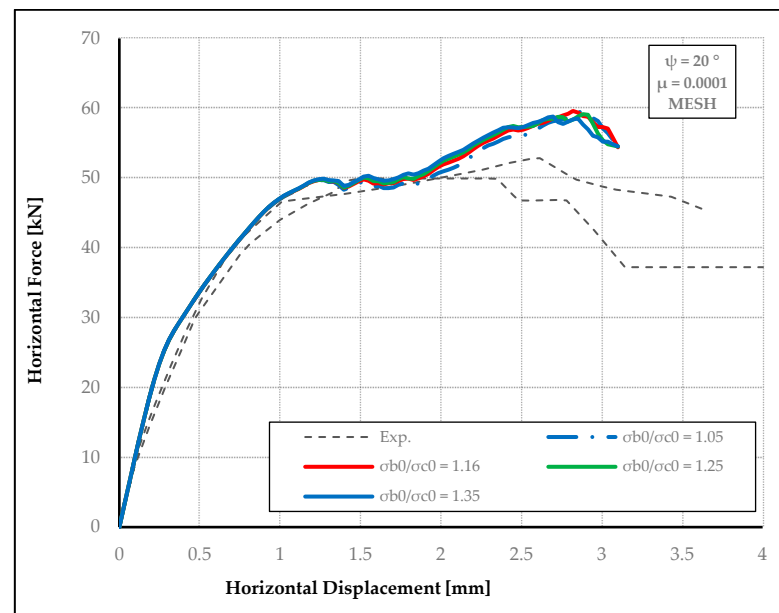


Figure 11. Capacity curves obtained from the analysis of micro-models with dilation angle equal to 20° for different ratios between compressive yielding stresses.

5.1.5. Remarks about the Sensitivity Analysis

The aim was to carry out a sensitivity analysis for some of the parameters of the CDP to understand how a change in the input data of this constitutive law affects the output and provide some suggestions for the calibration of these parameters for micro-model analysis of masonry structures. Moreover, it was also possible to identify the particular set of parameters that allow one to simulate the behavior of the J4D and J5D Eindhoven panels.

The analyses have shown that the models with the best fit are those corresponding to the dilation angle equal to 20° in Figure 8 and the one corresponding to MESH + in Figure 9b (characterized by a dilation angle equal to 15°). The first model (Table 8) has been used in the following sections to evaluate the influence of the tensile behavior and boundary conditions on the shear response of the panel. This model has been chosen in order to reduce the computational effort.

Table 8. The set of parameters for which the best fit with the benchmark test has been achieved.

Fixed Parameters			
ψ [°]	μ	σ_{b0}/σ_{c0}	Mesh size [cm]
20°	0.0001	1.16	3.00 (MESH)

From the sensitivity analysis, it has been possible to observe that the viscosity parameter considerably influences the masonry response. While a higher value avoids convergence issues and guarantees a smoother response curve, on the other hand, it leads to considerable overstrength that is not truly related to the material mechanical behavior. Therefore, to avoid the overestimation of strength, the viscosity parameter value should be kept as low as possible. Similarly, the dilation angle, especially in the case of confined masonry, can considerably affect the shear response, leading to additional prestressing that results in overstrength. This parameter should be then opportunely calibrated against a specific experimental test on masonry that provides an estimation of the material dilation. Finally, the influence of the ratio between the compressive stresses, although correlated to the slope of the yield surface in the p - q plane, seems to be negligible. It is likely that its influence is more relevant for higher prestressing loads.

5.2. Tensile Behavior

For the tensile response of concrete, a multilinear law is usually adopted [71]. Similarly, here, different from the previous sections, a bilinear law has been implemented for the tensile response of both the mortar and the masonry units. Different laws have been adopted, changing the ratio between the total fracture energy G_F and the initial one G_f and the ratio between the maximum tension f' and the corner tension s (see Figure 12).

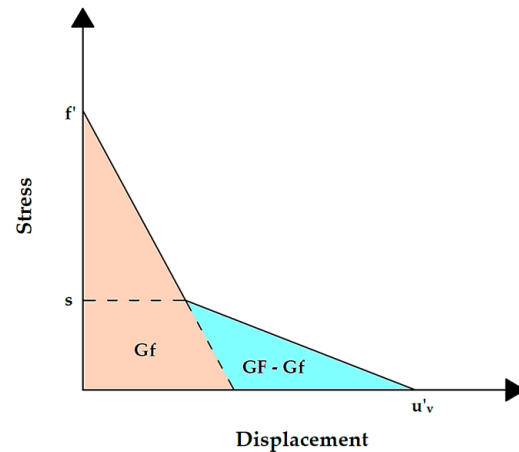


Figure 12. Bilinear relationship for the tensile behavior.

The total fracture energy has, instead, been kept constant (see Tables 9–12 for the obtained laws). For the purposes of the analyses, six models have been implemented: Three analyze the influence of the s/f' ratio and three analyze the influence of the G_F/G_f ratio, both for the units and the mortar. The set of parameters reported in Table 13 has been kept constant, whereas the tensile response has been varied.

Table 9. Parameters set to analyze the influence of the s/f' ratio for the units.

Bilinear Laws for Blocks Assumed to Analyze the Influence of the s/f' ratio				
Parameters				
f' [Pa]	G_F [J/m]	G_f [J/m]	G_F/G_f	s/f'
2,000,000	80	32	2.50	0.20; 0.10; 0.05
Implemented laws				
s/f'	Data		Sub-options	
	Tensile strength [Pa]	Displacement [m]	Damage Parameter	Displacement [m]
0.20	2,000,000	0	0	0
	400,000	0.0000256	0.1	0.000272
	0	0.0002720	>>	>>
0.10	2,000,000	0	0	0
	200,000	0.0000288	0.1	0.000512
	0	0.0005120	>>	>>
0.05	2,000,000	0	0	0
	100,000	0.0000304	0.1	0.000992
	0	0.0009920	>>	>>

Table 10. Parameters set to analyze the influence of the s/f' ratio for the mortar.

Bilinear Laws for Mortar to Analyze the Influence of the s/f' Ratio				
Parameters				
f' [Pa]	G_F [J/m]	G_f [J/m]	G_F/G_f	s/f'
250,000	18	7.20	2.50	0.20; 0.10; 0.05
Implemented laws				
s/f'	Data		Sub-options	
	Tensile strength [Pa]	Displacement [m]	Damage Parameter	Displacement [m]
0.20	250,000	0	0	0
	50,000	0.00004608	0.1	0.0004896
	0	0.00048960	>>	>>
0.10	250,000	0	0	0
	25,000	0.00005184	0.1	0.0009216
	0	0.00092160	>>	>>
0.05	250,000	0	0	0
	12,500	0.00005472	0.1	0.0017856
	0	0.00178560	>>	>>

Table 11. Parameters set to analyze the influence of the G_F/G_f ratio for the units.

Bilinear Laws for Blocks to Analyze the Influence of the G_F/G_f Ratio				
Parameters				
f' [Pa]	G_F [J/m]	G_f [J/m]	G_F/G_f	s/f'
2,000,000	80	26.67; 20.00; 16.00	3.00; 4.00; 5.00	0.33
Implemented laws				
G_F/G_f	Data		Suboptions	
	Tensile strength [Pa]	Displacement [m]	Damage Parameter	Displacement [m]
3.00	2,000,000	0	0	0
	66,666.67	0.0000177778	0.1	0.000186667
	0	0.0001866667	>>	>>
4.00	2,000,000	0	0	0
	666,666.67	0.0000133333	0.1	0.0002
	0	0.0002000000	>>	>>
5.00	2,000,000	0	0	0
	666,666.67	0.0000106667	0.1	0.000208
	0	0.0002080000	>>	>>

Table 12. Parameters set to analyze the influence of the G_F/G_f ratio for the mortar.

Bilinear Laws for Mortar to Analyze the Influence of the G_F/G_f Ratio				
Parameters				
f' [Pa]	G_F [J/m]	G_f [J/m]	G_F/G_f	s/f'
250,000	18	6.00; 4.50; 3.60	3.00; 4.00; 5.00	0.33
Implemented laws				
G_F/G_f	Data		Suboptions	
	Tensile strength [Pa]	Displacement [m]	Damage Parameter	Displacement [m]
3.00	250,000	0	0	0
	83,333.33	0.0000320	0.1	0.000336
	0	0.0003360	>>	>>
4.00	250,000	0	0	0
	83,333.33	0.0000240	0.1	0.00036
	0	0.0003600	>>	>>
5.00	250,000	0	0	0
	83,333.33	0.0000192	0.1	0.0003744
	0	0.0003744	>>	>>

Table 13. Parameters set to analyze the influence of the bilinear tensile behavior.

Fixed Parameters			
ψ [°]	μ	σ_{b0}/σ_{c0}	Mesh size [cm]
20°	0.0001	1.16	3.00 (MESH)

Figure 13 shows that the yielding point does not change with the tensile curve. A slight variation is instead shown in the post-elastic response, with higher hardening or ductility for higher values of s/f' or lower values of G_F/G_f . The small variation in the results might be explained by the fact that the damaged areas of the panel are limited, hence a small variation of the tensile laws cannot affect the results considerably. Nevertheless, the curves are within the range of the experimental envelope and, in the post-elastic range, are lower than the one obtained with a linear law. Hence, it can be concluded that all the bilinear laws offer a better fit of the experimental results, and, in particular, the green curve in Figure 13a (with $G_F/G_f = 2.5$ and $s/f' = 0.2$) almost perfectly follows the lower curve of the benchmark.

5.3. Influence of the Boundary Conditions

5.3.1. Prestressing Load

To validate the set of parameters (Table 14), additional tests of the experimental campaign have been modeled. The analyses have been repeated for higher vertical loads, coherently with the values adopted for the experimental panels J6D and J7D (see Table 15).

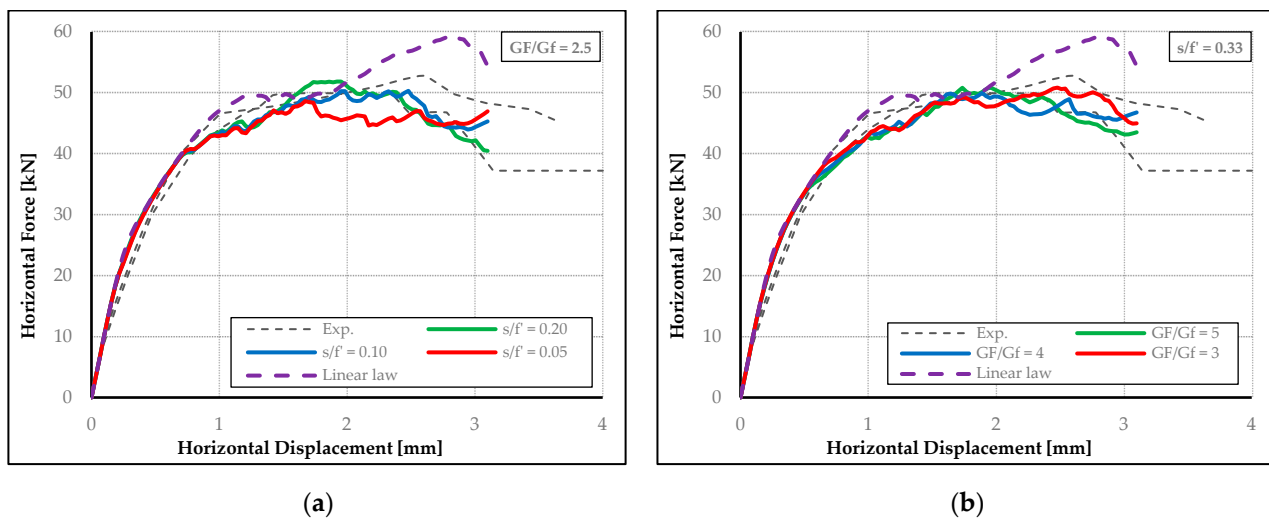


Figure 13. Capacity curves obtained for micro-models with different tensile curves: (a) $r_{GF/G_f} = 2.5$; $s/f' = \text{variable}$; (b) $s/f' = 0.33$; G_F/G_f ratio = variable.

Table 14. Parameters adopted to analyze the influence of the prestressing load, referred to as the micro-model with dilation angle of 20° .

Fixed Parameters			
$\psi [^\circ]$ 20°	μ 0.0001	σ_{b0}/σ_{c0} 1.16	Mesh size [cm] 3.00 (MESH)

Table 15. Values considered of the prestressing load.

Prestressing Load p		
J4D & J5D 0.30 MPa	J6D 1.21 MPa	J7D 2.12 MPa

The response curves shown in Figure 14 reproduce the experimental results for all the analyzed cases well, although with some reasonable differences, and this outcome further validates the calibrated set of parameters. Furthermore, the same figure shows how the response curve changes with the prestressing load. By increasing the prestressing load, the first yielding force becomes higher, coherently with the yielding surface shape, whereas the softening branch becomes more pronounced.

The damage maps obtained also reproduce the experimental results well, with a similar diagonal damage pattern becoming more widespread as the prestressing load becomes bigger, progressively affecting more blocks and more mortar joints (see Figure 15). The increase in the damaged area, with the reduction of the possible alternative load paths, could explain the more pronounced softening under the higher prestressing loads.

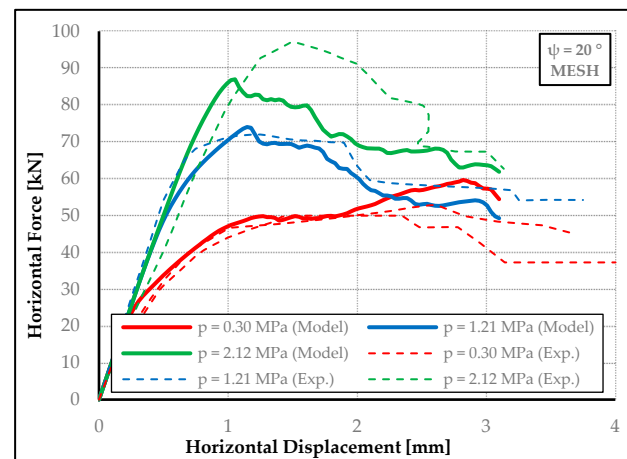


Figure 14. Experimental and numerical capacity curve (model with the parameters of Table 14), with different prestressing loads.

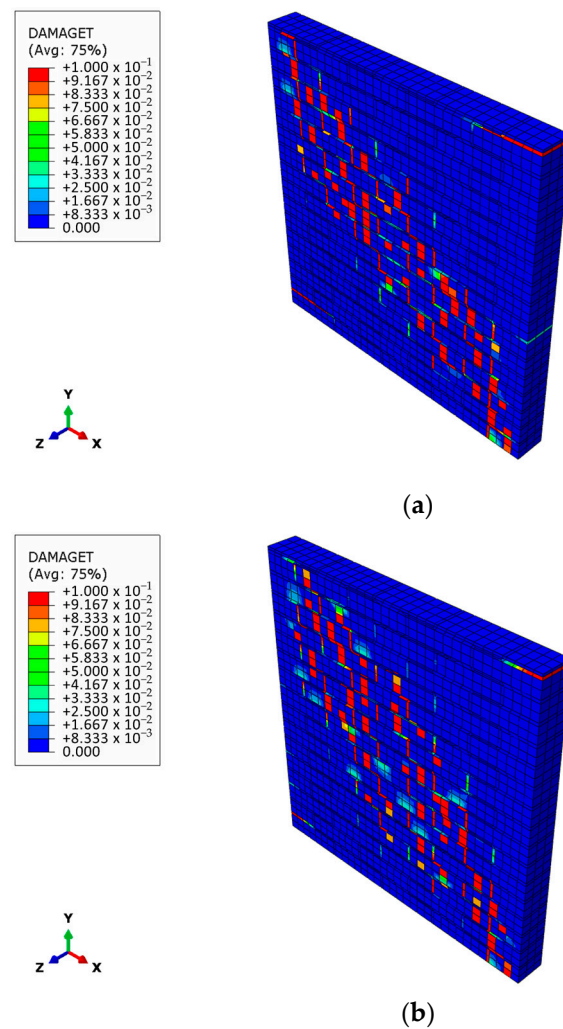


Figure 15. Damage map of the model with the parameters of Table 14: (a) Prestressing load of 1.21 MPa; (b) prestressing load of 2.12 MPa.

5.3.2. Influence of the Boundary Conditions at the Top

In this section, in order to study the influence of dilatancy on the model response, the displacement constraints at the top of the panel have been removed.

As can be seen from the curves in Figure 16, differently from what has been observed in Section 5.1.1, there are no significant differences between the curves obtained for different values of the dilation angle. This is coherent with the hypothesis that the increase in strength associated with dilatancy was related to the presence of constraints, which lead to additional precompression. In all cases, the models reach the collapse at very low load values when compared to experimental results. This can be explained by observing the deformed shape because the top face is now free to move, and the failure is reached not by the development of diagonal cracking (as in the previous cases) but by a hybrid failure mechanism combining overturning and shearing-sliding, as can also be seen from the damage maps (Figure 17).

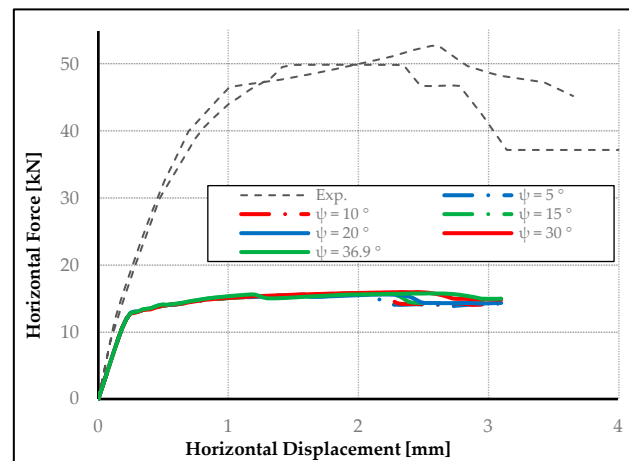


Figure 16. Capacity curves obtained from the analysis of micro-models without boundary conditions applied at the top and different dilation angles.

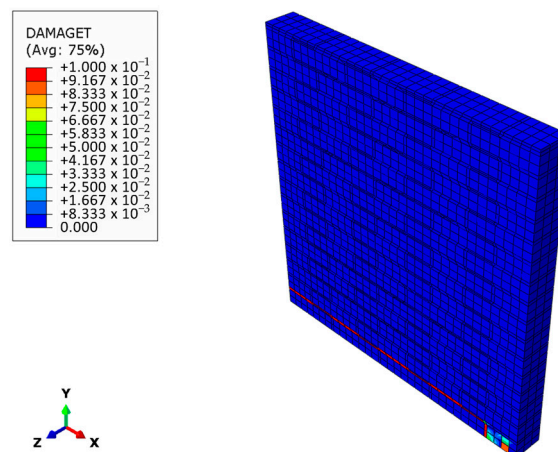


Figure 17. Typical crack pattern observed for micro-models without boundary conditions applied to the top.

6. Sensitivity Analysis for the Macro-Model Parameters

When dealing with the homogeneous model, the number of parameters to calibrate increases. In fact, for example, elastic parameters are also now apriori unknown. Furthermore, differently from the micro-models, it is harder to refer to experimental or literature values even for the material strength, because, for example, tensile tests are not usually conducted on whole masonry panels. In this section, leaving aside elastic parameters, which have already been calibrated while fitting the first branch of the response curve, the influence of some other CDP parameters is studied in order to calibrate the set of parameters that allows the correct reproduction of the experimental results. As in the case

of the micro-model, thanks to the sensitivity analysis, it has been possible to identify the key CDP parameters for modeling masonry.

For the calibration of the CDP parameters, according to the experimental results, the following parameters have been varied:

1. Dilatancy.
2. Ratio of compressive yielding stresses.
3. Mesh size.
4. Tensile yield strength.

Table 16 reports the parameters adopted, highlighting the ones that will be varied in the next sections. For the tensile strength, the fracture energy has been assumed to be equal to that of the mortar, which is available from the experimental data.

Table 16. CDP parameters adopted for the homogeneous panel.

Concrete Damage Plasticity for Mortar					
Elasticity parameters	E [Pa] 3,128,000,000			ν 0.15	
Plasticity parameters	ψ [°] variable	ϵ_e 0.1	σ_{b0}/σ_{c0} variable	K 2/3	μ 0.0001
Compressive response	Compressive strength [Pa]	Inelastic strain [%]	Damage parameter	Inelastic strain [%]	
	13,000,000	0	0	0	
	17,500,000	0.004	0.1	0.005	
	0	0.01	0.2	0.015	
Tensile response	Tensile strength [Pa]	Cracking displacement [m]	Damage parameter	Cracking Displacement [m]	
	variable	0	0	0	
	0	variable	0.1	variable	

For the purposes of the analyses, fifteen models have been implemented: Six to analyze the influence of the dilation angle, four to investigate the ratio between yielding compressive stress, two for the effect of the mesh size, and three for the tensile yield strength.

6.1. Dilation Angle

First, as well as for the micro-model analyses, the influence of the dilation angle on the capacity curves has been analyzed (see Table 17 for the values considered). To analyze this aspect, some parameters have been selected, assuming for them the values reported in Table 18.

Table 17. Values assumed in the analyses for the dilation angle.

Dilation Angle ψ					
5°	10°	15°	20°	30°	36.9°

Table 18. Parameters that have been fixed to analyze the influence of the dilation angle.

Fixed Parameters		
σ_{b0}/σ_{c0}	Mesh size [cm]	Tensile yielding stress (displacement)
1.16	3.00 (MESH)	0.25 MPa (0.00015 m)

Figure 18 shows that the response obtained for the homogeneous models is very different if compared to the micro-models (Figure 7). Comparing the numerical results

with the experimental ones, although there is an initial “elastic” branch that follows the benchmark curve perfectly, very soon a very rapid strength decay is observed that rapidly brings the panel to an almost null resistance. In these models, the curve that is closer to the benchmark results is the one corresponding to the higher dilation angle, 36.9° , although too-high softening of the response is exhibited anyway. This difference in the response can be explained considering that in the micro-model, which is a more realistic and detailed representation of the physical reality, blocks are able to remain mostly elastic, allowing redistribution according to alternative load paths after the development of damage in mortar joints. This is not possible in the homogenized approach, in which, therefore, the softening behavior is more accentuated.

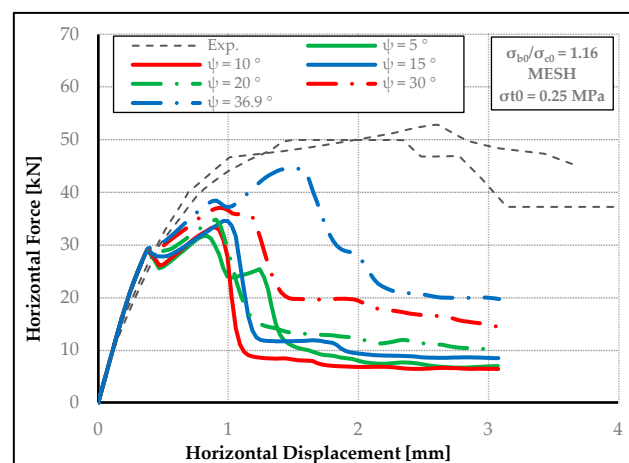


Figure 18. Capacity curves obtained from the analysis of macro-models changing the dilation angle.

With regard to other effects observed when varying the dilation angle, by increasing this value, it is seen that the post-elastic strength increases, similarly to the micro-model cases. Instead, no change in the elastic limit points is observed again, confirming that the dilation angle does not affect the yielding surface.

Figure 19 shows an example of the tensile damage map, with widespread diagonal cracking coupled with horizontal cracking at the two opposite corners, consistent with the experimental results.

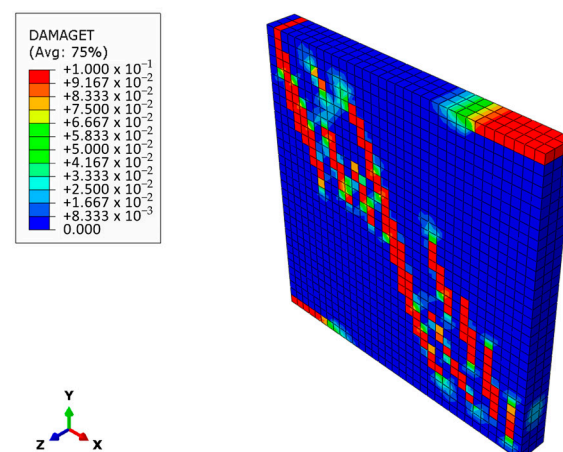


Figure 19. Typical crack pattern registered for macro-models with the coarse mesh (MESH).

6.2. Ratio between Compressive Yielding Stresses

To assess the influence of the ratio between compressive uniaxial and equibiaxial yielding stresses, σ_{b0}/σ_{c0} , on the behavior of the panel, the model with a dilation angle of 20° has been considered (Table 19), assuming the values reported in Table 20.

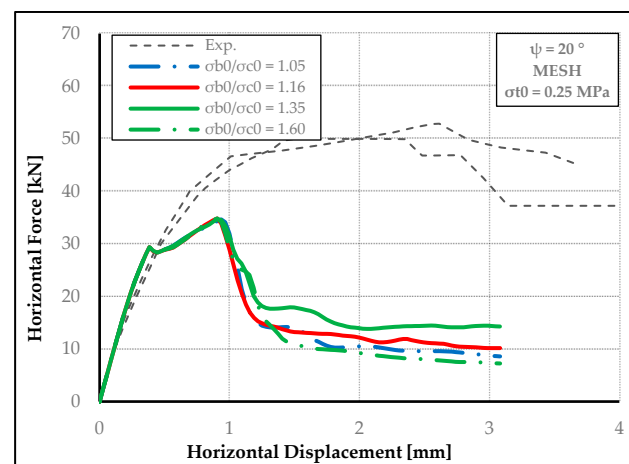
Table 19. Parameters set to analyze the influence of the ratio between yielding stresses.

Fixed Parameters		
ψ [°]	Mesh size [cm]	Tensile yielding stress (displacement)
20°	3.00 (MESH)	0.25 MPa (0.00015 m)

Table 20. Values considered for the ratio between compressive yielding stresses.

Ratio σ_{b0}/σ_{c0}			
1.05	1.16	1.35	1.60

Figure 20 shows the force displacement curves obtained. Similar to the micro-modeling approach, the σ_{b0}/σ_{c0} parameter does not significantly affect the force–displacement curves (see Figure 11). The slope of the yielding surface in the p–q plane does not influence the results, likely because the vertical prestressing load is very low.

**Figure 20.** Capacity curves of macro-models for different ratios σ_{b0}/σ_{c0} .

6.3. Sensitivity to the Mesh Size

To assess the influence of the mesh size on the behavior of the panel, the model with a dilation angle of 36.9° has been considered (Table 21).

Table 21. Parameters set to analyze the influence of the mesh size.

Fixed Parameters		
ψ [°]	σ_{b0}/σ_{c0}	Tensile yielding stress (displacement)
36.9°	1.16	0.25 MPa (0.00015 m)

Figure 21 shows that by varying the mesh size, a considerable change in the softening branch is observed for the capacity curves. Until the peak strength is reached, the two curves corresponding to the coarse and fine mesh sizes (MESH and MESH+, respectively) almost overlap. After that, the MESH+ model exhibits a perfectly plastic response, without considerable strength losses. Instead, the MESH model shows a significant strength loss (approximately 50%). With regard to the tensile damage map, the diagonal damaged area obtained with the MESH+ (see Figure 22) is not widespread as in the case of the coarse mesh (Figure 19) but appears to be divided into three almost vertical bands. This damage pattern is quite different from the experimental one, but at the same time, could explain the higher post-elastic branch of the capacity curve, which is closer to the experimental response since it allows for the possibility of alternative load paths with consequently higher residual strength.

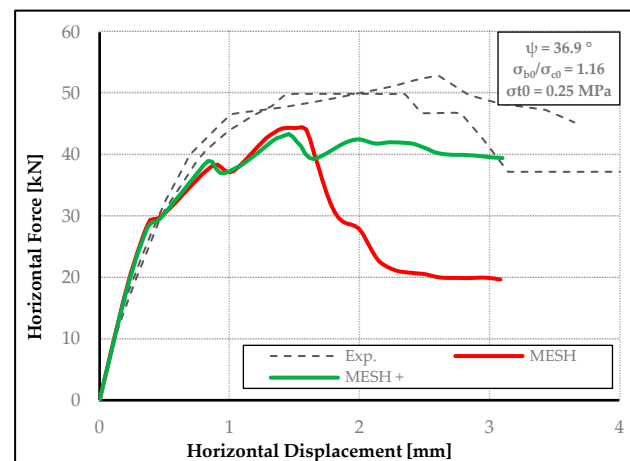


Figure 21. Response curves for two identical models with dilation angles equal to 36.9° that differ only regarding the mesh density.

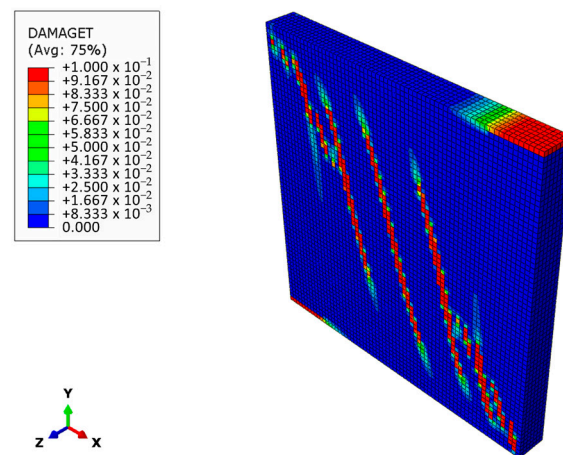


Figure 22. Damage map for the macro-models with the fine mesh (MESH+).

6.4. Tensile Yield Strength

Considering the differences between the numerical curves and the experimental ones, the analyses have been repeated by varying the tensile strength and keeping the variables of Table 22 fixed. In the previous analyses, the tensile strength was assumed to be equal to that of the mortar, which is the actual weak component that governs the masonry tensile response [72]. If the tensile strength is varied while fracture energy is kept constant, the ultimate tensile displacement decreases, and a more brittle behavior is assigned to masonry (Table 23).

Table 22. Parameters set to analyze the influence of the tensile behavior.

Fixed Parameters		
$\psi [^\circ]$ 36.9°	σ_{b0}/σ_{c0} 1.16	Mesh size [cm] 3.00 (MESH)

Table 23. Values considered of the tensile strength.

Tensile Strength σ_{t0}		
0.15 MPa (displacement = 0.00024 m)	0.25 MPa (displacement = 0.00015 m)	0.35 MPa (displacement = 0.0001028 m)

Figure 23 shows that the variation of the first tensile yielding stress considerably affects the response curves of the shear tests, and in fact, this effect is the most relevant point observed in the whole study. A higher tensile yield stress produces an increase in the capacity curve, demonstrating that under low prestress loads, the response curve is governed by cohesion, i.e., by the β parameter, which is the function of the tensile strength (Section 2.2). Comparing the curves with those of the benchmark, it is seen that, on average, better results have been obtained for values of tensile strength higher than those of the mortar. The best fitting curve is the one obtained with the value of 0.35 MPa, despite the overstrength observable in the initial branch (very slight) and in the final branch. The masonry texture provides a tensile overstrength compared to mortar alone, which can be taken into account at the macro scale by assuming a higher tensile strength.

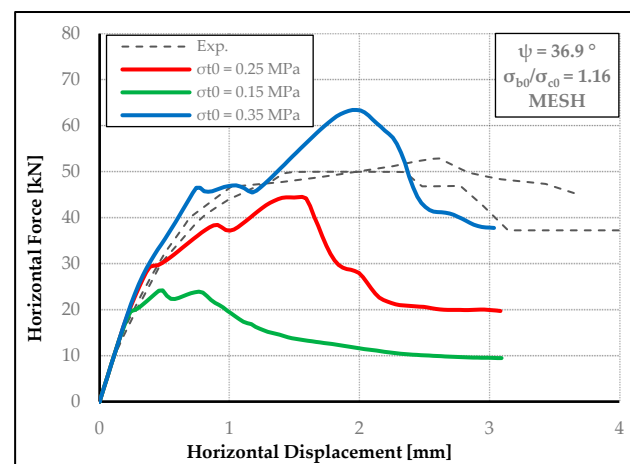


Figure 23. Response curves referring to the model shown in Table 22 with different tensile yielding stresses (Table 23).

6.5. Discussion of Results of the Sensitivity Analysis for the Macro-Model

With respect to the benchmark, the sensitivity analysis has allowed us to identify the set of parameters that provides the best fit of the parameters of the macro-model with the experimental results, especially in terms of the force–displacement curve (Table 24). It is interesting to observe that the effects of these parameters on the masonry behavior, from a general point of view, are similar to the micro-modeling approach discussed in the previous paragraphs. In detail, it has been seen that the compressive strength ratio has a negligible influence on the results, likely for the low precompression level of the benchmark tests; the dilation angle influences the post-elastic response but not the point of first yielding. With regard to the dilation angle, the calibrated parameter is higher than the one adopted for the micro-model. At the macro-scale, the dilation angle allows us to provide some extra strength to the model, recovering the coherence with the experimental results in which the high residual strength is related to the texture of masonry, which provides different load paths once certain mortar joints have been damaged. Furthermore, physically, the presence of the masonry texture can induce higher experimental dilatancy, such as in granular materials, and this explains the necessity of considering a higher value for the dilation angle for the homogeneous equivalent material.

Table 24. CDP parameters calibrated on the benchmark test.

Concrete Damage Plasticity for the Panel					
Elasticity parameters	E [Pa] 3,128,000,000			ν 0.15	
Plasticity parameters	ψ [°] 36.9	ϵ 0.1	σ_{b0}/σ_{c0} 1.16	K 2/3	μ 0.0001
Compressive response	Compressive strength [Pa]	Inelastic strain [%]	Damage parameter	Inelastic strain [%]	
	13,000,000	0	0	0	
	17,500,000	0.004	0.1	0.005	
	0	0.01	0.2	0.015	
Tensile response	Tensile strength [Pa]	Displacement [m]	Damage parameter	Displacement [m]	
	350,000	0	0	0.004	
	0	0.0001028	0.1	0.01	

With regard to the tensile behavior, the best fit has been obtained using a value of the tensile yielding strength more than twice the mortar, while keeping the tensile fracture energy equal to the mortar. The tensile strength is the parameter that influences the model response more relevantly through the “cohesion” parameter directly related to it. Of course, in the homogenization process, it is important to consider the influence on the response of the masonry units and their texture, which provides considerable residual strength.

In the end, in this case, the mesh size only influenced the post-peak response; with a finer mesh, the residual strength was almost equal to the peak, while the other model shows a decided reduction in the shear load-bearing capacity. This change in response can be explained by the different load paths for the finer mesh than for the experimental one.

7. Conclusions

Considering the experimental results obtained in Eindhoven on masonry panels under shear and vertical loads as a benchmark, a sensitivity analysis has been performed on the CDP parameters. For the analyses, both a micro-model and a homogeneous model have been adopted, comparing the two different modeling approaches and evaluating the possibility of adopting the micro-model to calibrate the parameters of the homogeneous model when the experimental data on masonry are not complete, which is a very frequent situation in practice.

The analyses have shown that the viscosity parameter considerably influences the results, with the possible occurrence of a fictitious overstrength, especially for high dilatancy and confined masonry. The dilation angle affects the results too, but only if the wall is constrained at the top and the vertical displacements are not allowed, resulting in an additional vertical prestress. In fact, in the unrestrained wall model, the response curve is insensitive to the dilation angle, which does not affect the yield surface but rather only the post-elastic deformations. The adoption of a bilinear tensile has allowed, in all cases, a better fit of the experimental results, coherently with what was observed for concrete. Finally, the tensile strength and its law, especially for low confining stresses, dominate the tensile response changing the cohesion of the material model.

In the end, it has been possible to understand the key parameters to be considered in a calibration procedure of CDP parameters, pointing out the subset of parameters that have a greater influence on the results than others. In a numerical procedure, it is always fundamental to preserve the physical meaning of parameters and coefficients used, making rational assumptions by controlling their level of variation and influence on the final results through appropriate sensitivity analyses.

The study presented here has considered a specific typology of masonry and load conditions, and of course, for different masonry materials and constructive techniques, it is expected that different specific results will be obtained. Moreover, the numerical analyses

presented are focused on a specific constitutive model (CDP [60]), which is very popular and extensively used in the technical and scientific panorama, as can be seen from the rich bibliography on the subject. The pre-calibration procedure proposed is aimed at more rational and effective use of complex nonlinear constitutive models for masonry from the perspective of practical, real case-study applications, representing, in this sense, an indication of a methodological nature. The actual scope of the work presented, indeed, is not to obtain specific reference results but to define a general procedure that can be assumed to calibrate the most appropriate set of parameters for any case study, starting from a single experimental test, allowing us to overcome the lack of information that is typically encountered when dealing with existing buildings.

In the future, further applications and developments might be proposed both for the specific investigation of the CDP Model and for an extension of the reference results.

With regard to the first point, it could be interesting to apply the same procedure to further experimental tests on masonry panels with higher prestress loads in order to better highlight the possible effect of CDP parameters in real cases characterized by a combination of shear and high normal stresses. Furthermore, the masonry mechanical properties provided by the Italian National Code for certain masonry types, such as friction angle and cohesion, could be directly correlated to the CDP parameters.

An interesting continuation of the research could also contemplate the application of different software and constitutive models in order to offer a broader overview and allow a comparative evaluation of the performance and effectiveness of the most widespread solutions available in this field.

Author Contributions: Conceptualization, S.C., V.T. and G.U.; methodology, S.C., V.T. and G.U.; investigation, L.S.R., V.T., S.C. and G.U.; writing—original draft preparation, L.S.R. and V.T.; writing—review and editing, L.S.R., V.T. and G.U.; supervision, S.C., V.T. and G.U. All authors have read and agreed to the published version of the manuscript.

Funding: This research received no external funding.

Conflicts of Interest: The authors declare no conflict of interest.

References

1. Uva, G.; Greco, R.; Cundari, A.; Porco, F. La progettazione degli edifici in muratura: Criteri e regole generali. In *Fondamenti di Tecnica delle Costruzioni—Seconda Edizione*; Edizioni, C.S., Ed.; CittàStudi: Novara, Italy, 2021; pp. 687–726.
2. Endo, Y.; Miyoshi, K. Meso-scale numerical simulation of the mechanical behaviour of brick masonry in earth mortar. *J. Build. Eng.* **2023**, *74*, 106890. [\[CrossRef\]](#)
3. Gooch, L.J.; Masia, M.J.; Stewart, M.G.; Lam, C.Y. Statistical assessment of tensile and shear properties of unreinforced clay brick masonry. *Constr. Build. Mater.* **2023**, *386*, 131578. [\[CrossRef\]](#)
4. Lourenço, P.B. Computational Strategies for Masonry Structures. Ph.D. Thesis, Delft University of Technology, Delft, The Netherlands, 1996.
5. Lagomarsino, S.; Penna, A.; Galasco, A.; Cattari, S. TREMURI program: An equivalent frame model for the nonlinear seismic analysis of masonry buildings. *Eng. Struct.* **2013**, *56*, 1787–1799. [\[CrossRef\]](#)
6. Schiavoni, M.; Giordano, E.; Roscini, F.; Clementi, F. Advanced numerical insights for an effective seismic assessment of historical masonry aggregates. *Eng. Struct.* **2023**, *285*, 115997. [\[CrossRef\]](#)
7. Schiavoni, M.; Giordano, E.; Roscini, F.; Clementi, F. Numerical modeling of a majestic masonry structure: A comparison of advanced techniques. *Eng. Fail. Anal.* **2023**, *149*, 107293. [\[CrossRef\]](#)
8. Scacco, J.; Grillanda, N.; Milani, G.; Lourenço, P.B. Novel non-linear static numerical model for curved masonry structures based on a combined adaptive limit analysis and discrete FE computations. *Int. J. Solids Struct.* **2021**, *236–237*, 111265. [\[CrossRef\]](#)
9. Tateo, V.; Casolo, S. Explicit Dynamic Analysis by a Rigid Body-Spring Model of Impact Loads of Artillery on Middle Age Fortifications. *Buildings* **2021**, *11*, 607. [\[CrossRef\]](#)
10. D'altri, A.M.; Sarhosis, V.; Milani, G.; Rots, J.; Cattari, S.; Lagomarsino, S.; Sacco, E.; Tralli, A.; Castellazzi, G.; de Miranda, S. Modeling Strategies for the Computational Analysis of Unreinforced Masonry Structures: Review and Classification. *Arch. Comput. Methods Eng.* **2019**, *27*, 1153–1185. [\[CrossRef\]](#)
11. Murano, A.; Mehrotra, A.; Ortega, J.; Rodrigues, H.; Vasconcelos, G. Comparison of different numerical modelling approaches for the assessment of the out-of-plane behaviour of two-leaf stone masonry walls. *Eng. Struct.* **2023**, *291*, 116466. [\[CrossRef\]](#)
12. Roca, P.; Cervera, M.; Gariup, G.; Pelà, L. Structural Analysis of Masonry Historical Constructions. Classical and Advanced Approaches. *Arch. Comput. Methods Eng.* **2010**, *17*, 299–325. [\[CrossRef\]](#)

13. Lagomarsino, S.; Cattari, S. PERPETUATE guidelines for seismic performance-based assessment of cultural heritage masonry structures. *Bull. Earthq. Eng.* **2014**, *13*, 13–47. [[CrossRef](#)]
14. Page, A.W. Finite Element Model for Masonry. *J. Struct. Div.* **1978**, *104*, 1267–1285. [[CrossRef](#)]
15. Dolatshahi, K.M.; Yekrangnia, M. Out-of-plane strength reduction of unreinforced masonry walls because of in-plane damages. *Earthq. Eng. Struct. Dyn.* **2015**, *44*, 2157–2176. [[CrossRef](#)]
16. Minga, E.; Macorini, L.; Izzuddin, B.A. A 3D mesoscale damage-plasticity approach for masonry structures under cyclic loading. *Meccanica* **2017**, *53*, 1591–1611. [[CrossRef](#)]
17. D'Altri, A.M.; Messali, F.; Rots, J.; Castellazzi, G.; de Miranda, S. A damaging block-based model for the analysis of the cyclic behaviour of full-scale masonry structures. *Eng. Fract. Mech.* **2019**, *209*, 423–448. [[CrossRef](#)]
18. Nie, Y.; Sheikh, A.; Visintin, P.; Griffith, M. A robust computational strategy for failure prediction of masonry structures using an improved multi-surface damage-plastic based interface model. *Int. J. Numer. Methods Eng.* **2023**, *124*, 2498–2528. [[CrossRef](#)]
19. Cuomo, M.; Ventura, G. A complementary energy formulation of no tension masonry-like solids. *Comput. Methods Appl. Mech. Eng.* **2000**, *189*, 313–339. [[CrossRef](#)]
20. Bruggi, M.; Taliencio, A. Analysis of no-tension structures under monotonic loading through an energy-based method. *Comput. Struct.* **2015**, *159*, 14–25. [[CrossRef](#)]
21. Berto, L.; Saetta, A.; Scotta, R.; Vitaliani, R. An orthotropic damage model for masonry structures. *Int. J. Numer. Methods Eng.* **2002**, *55*, 127–157. [[CrossRef](#)]
22. Pelà, L.; Cervera, M.; Roca, P. An orthotropic damage model for the analysis of masonry structures. *Constr. Build. Mater.* **2013**, *41*, 957–967. [[CrossRef](#)]
23. Degli Abbatì, S.; D'Altri, A.M.; Ottonelli, D.; Castellazzi, G.; Cattari, S.; de Miranda, S.; Lagomarsino, S. Seismic assessment of interacting structural units in complex historic masonry constructions by nonlinear static analyses. *Comput. Struct.* **2019**, *213*, 51–71. [[CrossRef](#)]
24. Lopez, J.; Oller, S.; Onate, E.; Lubliner, J. A homogeneous constitutive model for masonry. *Int. J. Numer. Methods Eng.* **1999**, *46*, 1651–1671. [[CrossRef](#)]
25. Pantò, B.; Cannizzaro, F.; Caddemi, S.; Calì, I. 3d microelement modelling approach for seismic assessment of historical masonry churches. *Adv. Eng. Softw.* **2016**, *97*, 40–59. [[CrossRef](#)]
26. Zucchini, A.; Lourenço, P.B. A micro-mechanical homogenisation model for masonry: Application to shear walls. *Int. J. Solids Struct.* **2009**, *46*, 871–886. [[CrossRef](#)]
27. Brasile, S.; Casciaro, R.; Formica, G. Multilevel approach for brick masonry walls—Part I: A numerical strategy for the nonlinear analysis. *Comput. Methods Appl. Mech. Eng.* **2007**, *196*, 4934–4951. [[CrossRef](#)]
28. Milani, G.; Zuccarello, F.A.; Olivito, R.S.; Tralli, A. Heterogeneous upper-bound finite element limit analysis of masonry walls out-of-plane loaded. *Comput. Mech.* **2007**, *40*, 911–931. [[CrossRef](#)]
29. Bertolesi, E.; Milani, G.; Casolo, S. Homogenization towards a mechanistic Rigid Body and Spring Model (HRBSM) for the non-linear dynamic analysis of 3D masonry structures. *Meccanica* **2018**, *53*, 1819–1855. [[CrossRef](#)]
30. Marfia, S.; Sacco, E. Multiscale damage contact-friction model for periodic masonry walls. *Comput. Methods Appl. Mech. Eng.* **2012**, *205–208*, 189–203. [[CrossRef](#)]
31. Massart, T.J.; Peerlings, R.H.J.; Geers, M.G.D. An enhanced multi-scale approach for masonry wall computations with localization of damage. *Int. J. Numer. Methods Eng.* **2007**, *69*, 1022–1059. [[CrossRef](#)]
32. Leonetti, L.; Greco, F.; Trovalusci, P.; Luciano, R.; Masiani, R. A multiscale damage analysis of periodic composites using a couple-stress/Cauchy multidomain model: Application to masonry structures. *Compos. Part B Eng.* **2018**, *141*, 50–59. [[CrossRef](#)]
33. Koocheki, K.; Pietruszczak, S. Numerical analysis of large masonry structures: Bridging meso and macro scales via artificial neural networks. *Comput. Struct.* **2023**, *282*, 107042. [[CrossRef](#)]
34. Lourenço, P.B.; Rots, J.G.; Blaauwendraad, J. Continuum Model for Masonry: Parameter Estimation and Validation. *J. Struct. Eng.* **1998**, *124*, 642–652. [[CrossRef](#)]
35. Lourenço, P.B.; De Borst, R.; Rots, J.G. A plane stress softening plasticity model for orthotropic materials. *Int. J. Numer. Methods Eng.* **1997**, *40*, 4033–4057. [[CrossRef](#)]
36. Candoni, C.; Diana, L.; Formisano, A.; Rodrigues, H.; Vicente, R. Failure mechanisms and behaviour of adobe masonry buildings: A case study. *Eng. Fail. Anal.* **2023**, *150*, 107343. [[CrossRef](#)]
37. Casolo, S. Macroscopic modelling of structured materials: Relationship between orthotropic Cosserat continuum and rigid elements. *Int. J. Solids Struct.* **2006**, *43*, 475–496. [[CrossRef](#)]
38. De Bellis, M.L.; Addessi, D. A Cosserat Based Multi-Scale Model For Masonry Structures. *Int. J. Multiscale Comput. Eng.* **2011**, *9*, 543–563. [[CrossRef](#)]
39. Lubliner, J.; Oliver, J.; Oller, S.; Onate, E. A plastic-damage model for concrete. *Int. J. Solids Struct.* **1989**, *25*, 299–326. [[CrossRef](#)]
40. Lee, J.; Fenves, G.L. Plastic-Damage Model for Cyclic Loading of Concrete Structures. *J. Eng. Mech.* **1998**, *124*, 892–900. [[CrossRef](#)]
41. Temsah, Y.; Jahami, A.; Khatib, J.; Sonebi, M. Numerical Derivation of Iso-Damaged Curve for a Reinforced Concrete Beam Subjected to Blast Loading. *MATEC Web Conf.* **2018**, *149*, 02016. [[CrossRef](#)]
42. Temsah, Y.; Jahami, A.; Khatib, J.; Sonebi, M. Numerical analysis of a reinforced concrete beam under blast loading. *MATEC Web Conf.* **2018**, *149*, 02063. [[CrossRef](#)]

43. Casolo, S.; Biolzi, L.; Carvelli, V.; Barbieri, G. Testing masonry blockwork panels for orthotropic shear strength. *Constr. Build. Mater.* **2019**, *214*, 74–92. [\[CrossRef\]](#)
44. Nie, Y.; Sheikh, A.; Visintin, P.; Griffith, M. An interfacial damage-plastic model for the simulation of masonry structures under monotonic and cyclic loadings. *Eng. Fract. Mech.* **2022**, *271*, 108645. [\[CrossRef\]](#)
45. Rotunno, T.; Fagone, M.; Ranocchiai, G.; Grande, E. Micro-mechanical FE modelling and constitutive parameters calibration of masonry panels strengthened with CFRP sheets. *Compos. Struct.* **2022**, *285*, 115248. [\[CrossRef\]](#)
46. Hernoune, H.; Benabed, B.; Abousnina, R.; Alajmi, A.; Alfadhili, A.M.G.; Shalwan, A. Experimental Research and Numerical Analysis of CFRP Retrofitted Masonry Triplets under Shear Loading. *Polymers* **2022**, *14*, 3707. [\[CrossRef\]](#)
47. Huang, D.; Albareda, A.; Pons, O. Experimental and Numerical Study on Unreinforced Brick Masonry Walls Retrofitted with Sprayed Mortar under Uniaxial Compression. *Buildings* **2023**, *13*, 122. [\[CrossRef\]](#)
48. Nastri, E.; Todisco, P. Macromechanical Failure Criteria: Elasticity, Plasticity and Numerical Applications for the Non-Linear Masonry Modelling. *Buildings* **2022**, *12*, 1245. [\[CrossRef\]](#)
49. Bayraktar, A.; Hökelekli, E.; Yang, T.T. Seismic failure behavior of masonry domes under strong ground motions. *Eng. Fail. Anal.* **2022**, *142*, 106749. [\[CrossRef\]](#)
50. Cardinali, V.; Pintucchi, B.; Tanganelli, M.; Trovati, F. Settlement of masonry barrel vaults: An experimental and numerical study. *Procedia Struct. Integr.* **2023**, *44*, 1252–1259. [\[CrossRef\]](#)
51. Tariq, H.; Najafgholipour, M.A.; Sarhosis, V.; Milani, G. In-plane strength of masonry wall panels: A comparison between design codes and high-fidelity models. *Structures* **2023**, *47*, 1869–1899. [\[CrossRef\]](#)
52. Scamardo, M.; Zucca, M.; Crespi, P.; Longarini, N.; Cattaneo, S. Seismic Vulnerability Evaluation of a Historical Masonry Tower: Comparison between Different Approaches. *Appl. Sci.* **2022**, *12*, 11254. [\[CrossRef\]](#)
53. D'Altri, A.M.; Presti, N.L.; Grillanda, N.; Castellazzi, G.; de Miranda, S.; Milani, G. A two-step automated procedure based on adaptive limit and pushover analyses for the seismic assessment of masonry structures. *Comput. Struct.* **2021**, *252*, 106561. [\[CrossRef\]](#)
54. Ferrante, A.; Giordano, E.; Clementi, F.; Milani, G.; Formisano, A. FE vs. DE Modeling for the Nonlinear Dynamics of a Historic Church in Central Italy. *Geosciences* **2021**, *11*, 189. [\[CrossRef\]](#)
55. Papa, G.S.; Tateo, V.; Parisi, M.A.; Casolo, S. Seismic response of a masonry church in Central Italy: The role of interventions on the roof. *Bull. Earthq. Eng.* **2020**, *19*, 1151–1179. [\[CrossRef\]](#)
56. Milani, G.; Valente, M.; Fagone, M.; Rotunno, T.; Alessandri, C. Advanced non-linear numerical modeling of masonry groin vaults of major historical importance: St John Hospital case study in Jerusalem. *Eng. Struct.* **2019**, *194*, 458–476. [\[CrossRef\]](#)
57. Albu-Jasim, Q.; Papazafeiropoulos, G. A Neural Network Inverse Optimization Procedure for Constitutive Parameter Identification and Failure Mode Estimation of Laterally Loaded Unreinforced Masonry Walls. *Civileng* **2021**, *2*, 943–968. [\[CrossRef\]](#)
58. Rakić, D.M.; Bodić, A.S.; Miličević, N.J.; Dunić, V.L.; Živković, M.M. Concrete Damage Plasticity Material Model Parameters Identification. *J. Serbian Soc. Comput. Mech.* **2021**, *15*, 111–122. [\[CrossRef\]](#)
59. Lu, W.; Lubbad, R.; Løset, S.; Høyland, K. Cohesive Zone Method Based Simulations of Ice Wedge Bending: A Comparative Study of Element Erosion, CEM, DEM and XFEM. In Proceedings of the 21st IAHR International Symposium on Ice “Ice Research for a Sustainable Environment”, Dalian, China, 11–15 June 2012; Dalian University of Technology Press: Dalian, China, 2021; ISBN 978-7-89437-020-4.
60. Smith, M. *ABAQUS/Standard User's Manual, Version 2022*; Dassault Systèmes Simulia Corp.: Providende, RI, USA, 2022.
61. Voyiadis, G.Z.; Kattan, P.I.; Taqieddin, Z.N. Analysis of Damage in Composite Materials using Fabric Tensors and the Continuum Approach. In Proceedings of the McMat2005: Joint ASME/ASCE/SES Conference on Mechanics and Materials, Baton Rouge, LA, USA, 1–3 June 2005.
62. Kachanov, L. *Time of the Rupture Process under Creep Conditions*; Izvestia Akademii Nauk SSSR, Otdelenie Tekhnicheskikh Nauk: Moscow, Russia, 1958; Volume 8, pp. 26–31.
63. Rabotnov, Y.N. *Creep Problems in Structural Members*; Series in Applied Mathematics and Mechanics; North-Holland publishing company: Amsterdam, Netherland, 1969.
64. Hong, W.-K. Chapter 3—The investigation of the structural performance of the hybrid composite precast frames with mechanical joints based on nonlinear finite element analysis. In *Hybrid Composite Precast Systems*; Woodhead Publishing Series in Civil and Structural Engineering, Hybrid Composite Precast Systems; Woodhead Publishing: Sawston, UK, 2020; pp. 89–177. [\[CrossRef\]](#)
65. Șerban, D.-A.; Furtos, G.; Marșavina, L.; Șoșdean, C.; Negru, R. Numerical modelling of the mechanical behaviour of wood fibre-reinforced geopolymers. *Contin. Mech. Thermodyn.* **2020**, *35*, 957–969. [\[CrossRef\]](#)
66. Michał, S.; Andrzej, W. Calibration of the CDP model parameters in Abaqus. In Proceedings of the 2015 World Congress on Advances in Structural Engineering and Mechanics (ASEM15), Incheon, Republic of Korea, 25–29 August 2015.
67. Demir, A.; Ozturk, H.; Edip, K.; Stojmanovska, M.; Bogdanović, A. Effect of viscosity parameter on the numerical simulation of reinforced concrete deep beam behavior. *Online J. Sci. Technol.* **2018**, *8*, 50–56.
68. Raijmakers, T.M.J.; Vermeltfoort, A.T. *Deformation Controlled Tests in Masonry Shear Walls*; Report B-92-1156; TNO-Bouw: Delft, The Netherlands, 1992. (In Dutch)
69. Vermeltfoort, A.T.; Raijmakers, T.M.J. *Deformation Controlled Tests in Masonry Shear Walls*; Part 2; Report TUE/BKO/93.08; Eindhoven University of Technology: Eindhoven, The Netherlands, 1993. (In Dutch)

70. CUR. *Structural Masonry: An Experimental/Numerical Basis for Practical Design Rules*; Report 171; CUR: Gouda, The Netherlands, 1994. (In Dutch)
71. Bažant, Z.P. Concrete fracture models: Testing and practice. *Eng. Fract. Mech.* **2002**, *69*, 165–205. [[CrossRef](#)]
72. Van Der Pluijm, R. Shear Behaviour of bed joints. In Proceedings of the 6th North American masonry Conference, Philadelphia, PA, USA, 6–9 June 1993; pp. 125–136.

Disclaimer/Publisher’s Note: The statements, opinions and data contained in all publications are solely those of the individual author(s) and contributor(s) and not of MDPI and/or the editor(s). MDPI and/or the editor(s) disclaim responsibility for any injury to people or property resulting from any ideas, methods, instructions or products referred to in the content.